Site-selective photoinduced cleavage and profiling of DNA by chiral semiconductor nanoparticles

Maozhong Sun[1,2,6], Liguang Xu[1,2,6], Aihua Qu[1,2,6], Peng Zhao[3], Tiantian Hao[1,2], Wei Ma[1,2], Changlong Hao[1,2], Xiaodong Wen[3], Felippe M. Colombari[4], Andre F. de Moura[4], Nicholas A. Kotov [5], Chuanlai Xu [1,2] and Hua Kuang [1,2]*

Gene editing is an important genetic engineering technique that enables gene manipulation at the molecular level. It mainly relies on engineered nucleases of biological origin, whose precise functions cannot be replicated in any currently known abiotic artificial material. Here, we show that chiral cysteine-modified CdTe nanoparticles can specifically recognize and, following photonic excitation, cut at the restriction site GAT′ATC (′ indicates the cut site) in double-stranded DNA exceeding 90 base pairs, mimicking a restriction endonuclease. Although photoinduced reactive oxygen species are found to be responsible for the cleavage activity, the sequence selectivity arises from the affinity between cysteine and the conformation of the specific DNA sequence, as confirmed by quantum-chemical calculations. In addition, we demonstrate non-enzymatic sequence-specific DNA incision in living cells and in vivo using these CdTe nanoparticles, which may help in the design of abiotic materials for gene editing and other biological applications.

norganic biomimetic nanoparticles with intrinsic similarities of scale and conformation to biomolecules are considered the next generation of artificial enzymes[1–5]. Fundamental approaches to exploiting and screening the activities of nanozymes have been developed to support this interesting research direction[6–10], and the demand for a biomimetic DNA endonuclease in living cells is growing across the sciences[11–14].

DNA endonucleases are basic functional enzymes in biological systems that recognize and cleave specific DNA sequences at predetermined sites[15], making them significant tools for the physical mapping of chromosomes, nucleotide sequence analyses, target gene isolation and DNA recombination[16–19]. Artificial methods have been reported for the design of biomimetic restriction enzymes[7,20]. However, their cleavage site recognition still relies on engineered nucleotide sequences, and, so far, no known abiotic material with DNA targeting function has been achieved.

Semiconductor nanoparticles, also known as quantum dots, display surface-binding properties and size-dependent characteristics[21–31]. Based on previously reported specific interactions among chiral molecules and nanoparticles[32,33], cadmium telluride (CdTe) nanoparticles stabilized with cysteine (Cys, **1**) were used here as a biomimetic endonuclease for DNA scission (the proposed principle is presented in Fig. 1). Under illumination with either left- or right-handed circularly polarized light (CPL; LCP or RCP, respectively) provided by a 405 nm laser, the DNA was selectively cut by the nanoparticles between the T and A bases of the restriction site GATATC. Meanwhile, different ligands of CdTe nanoparticles were screened for specific cutting. Noticeably, the proposed artificial DNA endonuclease reaction was carried out well in living cells and in vivo.

Results and discussion
Chiral CdTe nanoparticle preparation and characterization.
We first synthesized water-soluble chiral nanoparticles. Truncated tetrahedral shape D- or L-Cys-modified CdTe nanoparticles with a diameter of 4.5 ± 0.3 nm were produced as described previously (Fig. 2a,b)[34]. Salmon sperm DNA, a natural double-stranded DNA of approximately 1,839 bp, which emits a circular dichroic (CD) signal at 200–320 nm (Supplementary Fig. 1), was used as cleavage substrate[35]. The D- and L-Cys-modified CdTe nanoparticles demonstrated broad mirror CD features between 350 and 410 nm (Fig. 2c and Supplementary Fig. 2). The L-Cys CdTe nanoparticles have a negative signal and the D-Cys CdTe nanoparticle signal is positive at these wavelengths. After the CdTe nanoparticles were mixed with DNA, the CD spectrum of the CdTe nanoparticles showed no obvious peak changes in the visible region (Supplementary Fig. 2)[36].

After the L-Cys CdTe–DNA mixture was illuminated with RCP for 2 h, the CD spectrum of the L-Cys CdTe showed distinct chiroptical activity at 365, 415, 470 and 488 nm, which are within the absorption bandgap transition (Fig. 2d and Supplementary Fig. 2). D-Cys CdTe combined with DNA and illuminated with LCP showed a corresponding mirror CD performance, demonstrating that CPL photons are capable of stimulating the reaction[37]. The accompanying geometric transformation was also examined with transmission electron microscopy (TEM), three-dimensional (3D) tomography and synchrotron small-angle X-ray scattering (Supplementary Figs. 3–5). The predominant products were nanorods with a total length of 20 ± 2 nm and total width of 5 ± 0.25 nm. The elemental Te content of the nanoparticles specifically increased after illumination for 2 h, which was confirmed with energy dispersive spectrometric mapping and inductively coupled plasma mass spectrometry (Supplementary Figs. 6 and 7). These results indicate the partial transformation of Te^{2-} to Te (Supplementary Fig. 8), which is consistent with previous reports[38]. The progression of nanorod formation with time was recorded with both CD spectroscopy and TEM. In the TEM images, the tetrahedral nanoparticles had an increased diameter (6 nm) after 0.5 h (Supplementary Figs. 9 and 10) and had evolved

[1]State Key Laboratory of Food Science and Technology, Jiangnan University, Wuxi, Jiangsu, China. [2]International Joint Research Laboratory for Biointerface and Biodetection, Jiangnan University, Wuxi, Jiangsu, China. [3]Institute of Coal Chemistry, Chinese Academy of Science, Taiyuan, Shanxi, China. [4]Department of Chemistry, Federal University of São Carlos, São Carlos, Brazil. [5]Department of Chemical Engineering, Biointerfaces Institute, University of Michigan, Ann Arbor, MI, USA. [6]These authors contributed equally: Maozhong Sun, Liguang Xu and Aihua Qu. *e-mail: kuangh@jiangnan.edu.cn
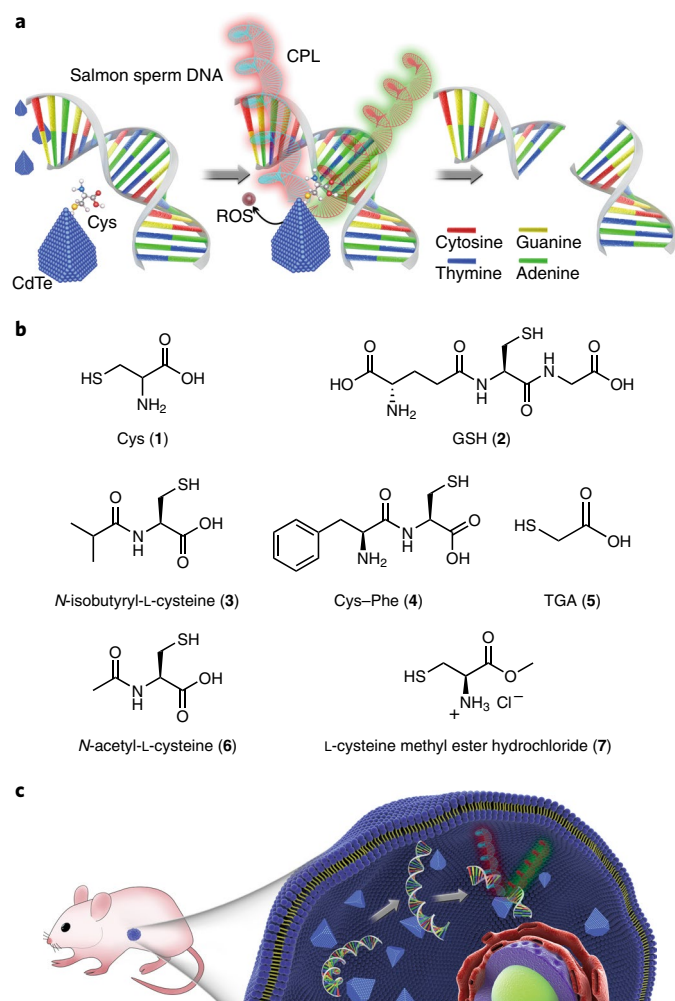
Fig. 1 | Strategy for site-selective DNA cleavage. a, Schematic illustration of chiral CdTe-based specific DNA cleavage under CPL irradiation. **b,** CdTe ligand screening for specific DNA cleavage. **c,** In vivo DNA cleavage by chiral CdTe nanoparticles. ROS, reactive oxygen species; GSH, glutathione; TGA, 2-mercapto acetic acid.

into elliptical nanoparticles at 1 h (Supplementary Figs. 11 and 12). When the irradiation time was extended to 1.5 h (Supplementary Figs. 13 and 14), the aspect ratio increased to 3.5, and the absorption peaks and CD signals were redshifted (Supplementary Fig. 15). During this process, the fluorescence of the solution changed from the initial wavelength of 620 nm to 630 nm, with reduced intensity, and there was a positive correlation between fluorescence intensity and the concentration of DNA substrate (Supplementary Fig. 16).

Ligands of CdTe nanoparticles, including glutathione (GSH, **2**), N-isobutyryl-L-cysteine (**3**), dipeptide (Cys-Phe, **4**), achiral 2-mercapto acetic acid (TGA, **5**), N-acetyl-L-cysteine (**6**) and L-cysteine methyl ester hydrochloride (**7**), were screened for DNA cutting (Fig. 2e–h). Interestingly, the CD signals from the nanoparticles in control groups did not differ before and after illumination, consistent with the TEM data (Supplementary Figs. 17–33). These results demonstrate that the chiral Cys ligand is an essential reactive species in the whole reaction process.

Site-selective DNA cleavage. The DNA scission activity of the chiral nanoparticles was analysed with agarose gel electrophoresis[39]. The original salmon sperm DNA used, registered in GenBank under accession no. NC_017838.1, has a 1,839 bp sequence

(Supplementary Table 1). On exposure to L-Cys CdTe under RCP illumination for 0.5 h, the DNA was gradually separated into different fragments (Fig. 3a). When the exposure period was increased to 1 h, weak bands representing two DNA fragments were apparent, arising from an incomplete reaction, but indicating a nuclease-like activity. After irradiation for 2 h, all the 1,839 bp DNA was completely separated into two distinct DNA fragments. A comparison of the electrophoretic image of the products after 5 h with earlier images demonstrated that the photoinduced cleavage reaction of the chiral nanoparticles was completed in 2 h. Like L-Cys CdTe, D-Cys CdTe displayed a strong DNA-cutting capacity at a specific DNA sequence (Fig. 3b), whereas the other ligands-modified CdTe had no obvious effect (Fig. 3g–i and Supplementary Figs. 34–36). This further confirmed that the Cys ligand on the CdTe surface plays a crucial role in DNA-specific cleavage.

To determine the cleavage site, the two DNA fragments were extracted from the gel and sequenced. Sequence-specific DNA cleavage occurred at the position between thymine (T, 1,083) and adenine (A, 1,084) (numbering from the 5′ end to the 3′ end). The sequenced lengths of the two fragments (1,083 bp and 756 bp) after nanoparticle digestion were consistent with the electrophoretic images (Supplementary Tables 2 and 3). To clarify the cutting property of the chiral nanoparticles, we first examined the influence of the DNA length. A 90 bp DNA fragment corresponding to a partial salmon sperm (1,839 bp) sequence containing the cutting site in the middle of the DNA was prepared (Supplementary Table 4). As shown in Fig. 3c, a DNA band of 45 bp was detected with electrophoresis after exposure. An 80 bp DNA fragment was not cut by the L-Cys nanoparticles during RCP illumination, although it had almost the same nucleotide sequence as the cut 90 bp DNA fragment (Fig. 3d). This was also observed when the D-Cys nanoparticles were combined with the 80 bp DNA under LCP, when no CD or morphological changes were observed (Supplementary Figs. 37–39). When the 90 bp DNA fragment was converted into a single strand with the same sequence, the electrophoretic band after the reaction was the same as the band before the reaction, indicating that only doubled-stranded DNA is cleaved by the CdTe endonuclease (Fig. 3e and Supplementary Figs. 40–42).

The band products from Fig. 3c were analysed by DNA sequencing, which showed that the 90 bp DNA was cut into 45 bp sections at the middle of the sequence between bases T and A, as shown in Supplementary Table 4. To screen the recognized sequence, series experiments with mutated DNA fragments were designed. We first changed the splicing sequences of the cutting site (AGAT″TACC). The chiral CdTe exerted no enzyme-like activity on the mutated DNA (Fig. 3f and Supplementary Figs. 43 and 44). We then prepared DNAs corresponding to the 90 bp sequence upstream or downstream from the cutting site, each of which contained half the original sequence. The CdTe shape in TEM images, the CD spectra and the electrophoretic bands remained unchanged (Supplementary Figs. 45–50). We then retained the DNA sequence upstream from the cutting site but created a point mutation in the downstream sequence. Interestingly, when the first three bases (with sequence ATC) were included, the corresponding DNA was cut by the chiral nanoparticles, with distinctive changes in their morphology and the corresponding CD shape (Supplementary Figs. 51–59). When the integrity of the downstream sequence was maintained, the DNA was cut when the upstream DNA sequence ended with bases GAT (Supplementary Figs. 60–68). Meanwhile, we tested DNA in which the sequences upstream and downstream from the target site were exchanged (ATCGAT). No CD or DNA cleavage effect was observed (Supplementary Figs. 69–74). Notably, the endonuclease developed here was stable under extreme conditions of 0 °C and 50 °C (Supplementary Figs. 75–76). These results show that the photoactive chiral CdTe nanoparticles have an unprecedented site-selective DNA cleavage capacity, with a target cleavage site between
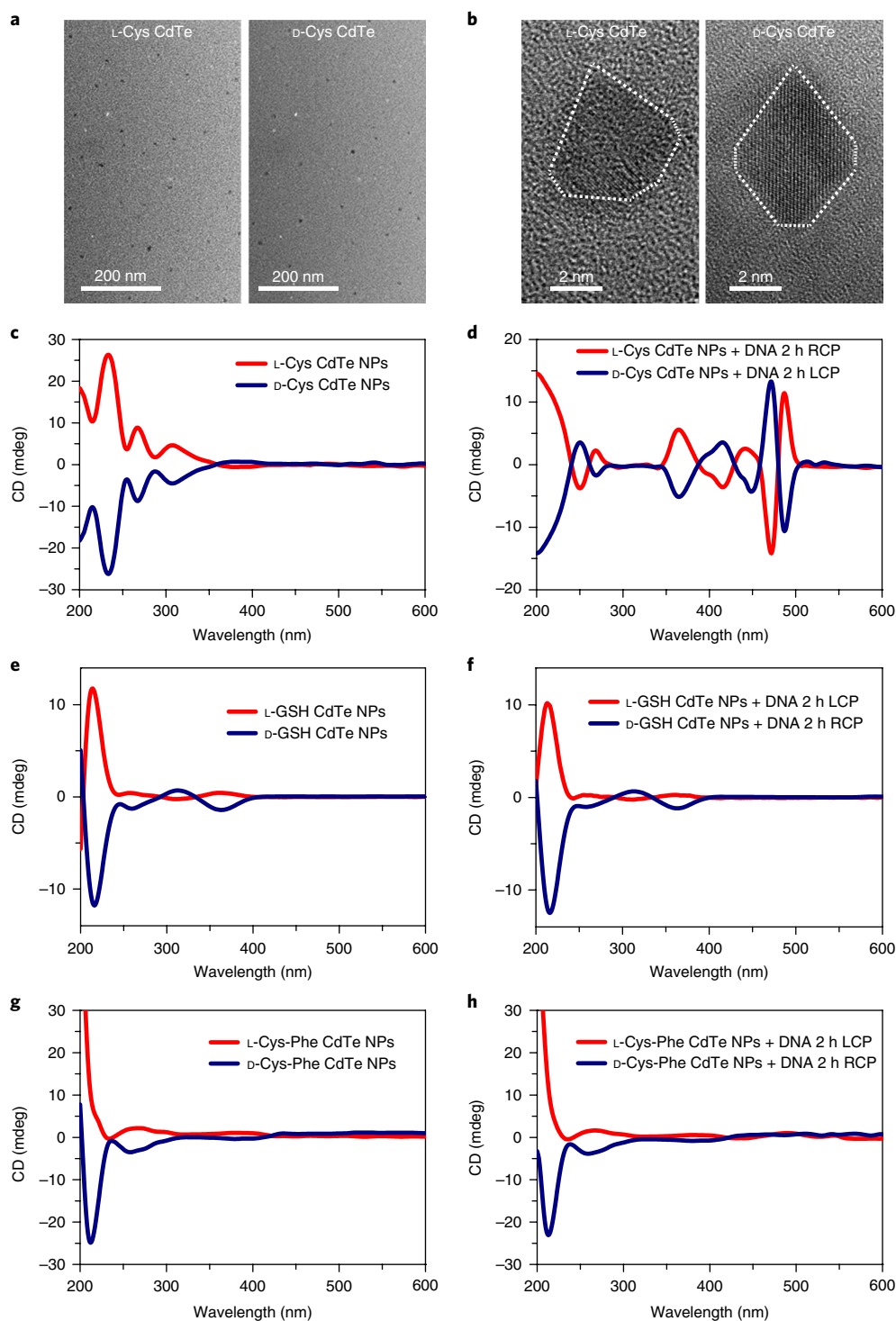
Fig. 2 | Chiral CdTe nanoparticle preparation and characterization. a,b, TEM (**a**) and high-resolution TEM (**b**) images of truncated tetrahedron-shaped (white dashed areas) L-Cys and D-Cys CdTe nanoparticles. **c,** CD spectra of L-Cys and D-Cys CdTe nanoparticles (NPs). **d,** CD spectra of L-Cys and D-Cys CdTe nanoparticles mixed with 1,839 bp DNA and illuminated under 405 nm RCP/LCP for 2 h. **e,f,** CD spectra of L-GSH and D-GSH CdTe nanoparticles before (**e**) and after (**f**) being mixed with 1,839 bp DNA and illuminated under 405 nm LCP/RCP for 2 h. **g,h,** CD spectra of L-Cys-Phe and D-Cys-Phe CdTe nanoparticles before (**g**) and after (**h**) being mixed with 1,839 bp DNA and illuminated under 405 nm LCP/RCP for 2 h. All experiments were performed in triplicate.

bases T and A in the GATATC recognition sequence from the 5′ end to the 3′ end, when the whole fragment length is over 90 bp (Supplementary Figs. 77–84).

Specific binding between the target DNA and chiral nanoparticles. To understand how CPL causes specific DNA cleavage, the

thermodynamic effect between DNA and the chiral CdTe nanoparticles was investigated with isothermal titration calorimetry (ITC)[30]. The interaction between L-Cys CdTe nanoparticles and the 90 bp DNA fragment showed a high affinity (binding constants of $(2.61 \pm 0.32) \times 10^5\,\mathrm{M}^{-1}$; Fig. 4a), and the D-Cys CdTe nanoparticles had a similar binding constant (Supplementary Figs. 85–87).
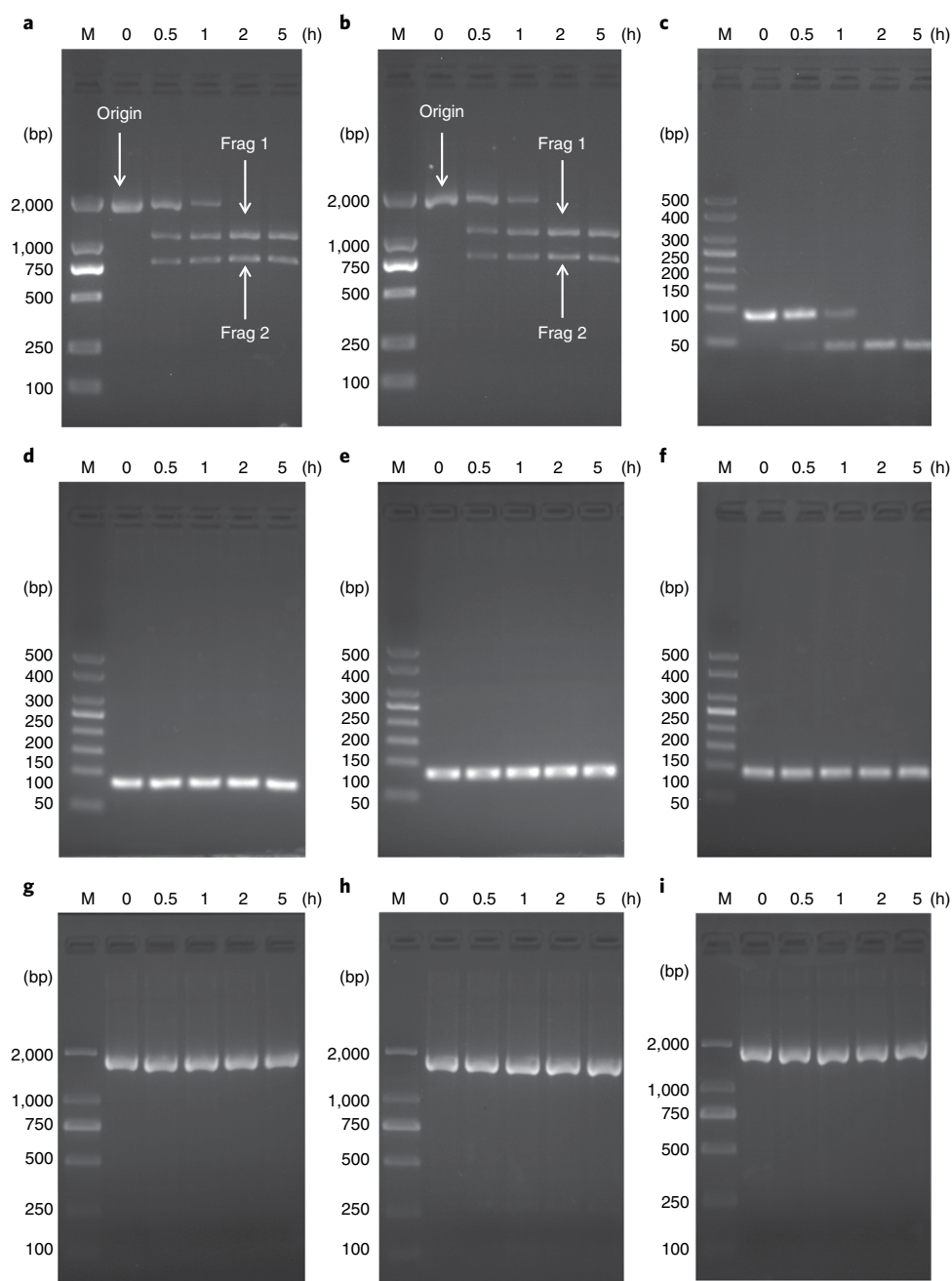
Fig. 3 | Site-selective DNA cleavage. a,b, Electrophoresis images of L-Cys CdTe (**a**) and D-Cys CdTe (**b**) nanoparticles with 1,839 bp DNA illuminated with 405 nm RCP/LCP for 2 h. The two DNA fragments after cleavage are denoted frag 1 and frag 2. **c–e,** Electrophoresis images of L-Cys CdTe nanoparticles with 90 bp (**c**), 80 bp (**d**) and single-stranded 90 bp (**e**) DNA, illuminated with 405 nm RCP for 2 h. **f,** L-Cys CdTe nanoparticles with mutated 90 bp DNA-1 illuminated with 405 nm RCP for 2 h. **g–i,** N-isobutyryl-L-cysteine-modified CdTe nanoparticles (**g**), N-acetyl-L-cysteine-modified CdTe nanoparticles (**h**) and L-cysteine methyl ester hydrochloride-modified CdTe nanoparticles (**i**) with 1,839 bp DNA illuminated with 405 nm RCP for 2 h. All experiments were performed in triplicate.

However, the 80 bp DNA ((4.13 ± 0.24) $\times 10^3 \, \text{M}^{-1}$) and the mutated DNA (($3.61 \pm 0.23$) $\times 10^3 \, \text{M}^{-1}$) showed limited affinity for the nanoparticles compared with that for the 90 bp DNA. Therefore, the association between the Cys-modified nanoparticles and the 90 bp DNA was stronger than for the other sequences. These experiments further confirm that DNA length and scission selectivity are essential elements of the developed cutting platform. Moreover, significant evidence from the transient absorption spectrum demonstrated that the recovery time of the nanoparticles was reduced after mixed with 90 bp DNA, which could facilitate the cutting reaction by accelerating electron transport (Fig. 4b and Supplementary

Figs. 88–90). This can be explained as follows. First, the nanoparticles showed a high affinity for the specific sequence in 90 bp DNA. Second, the alternating A and T bases are especially flexible, which is highly consistent with previous reports[40,41].

The specific cutting process was persuasively verified by changing the location of the recognition sequence (GAT′ATC) in the 90 bp DNA (Fig. 4c–g and Supplementary Fig. 91). Mutated 90 bp DNA fragments with the recognition sequence GAT′ATC located at the 5′ end or 3′ end, were constructed, respectively. After 2 h illumination with nanoparticles, the electrophoretic band and CD spectrum had not changed relative to those when the recognition sequence
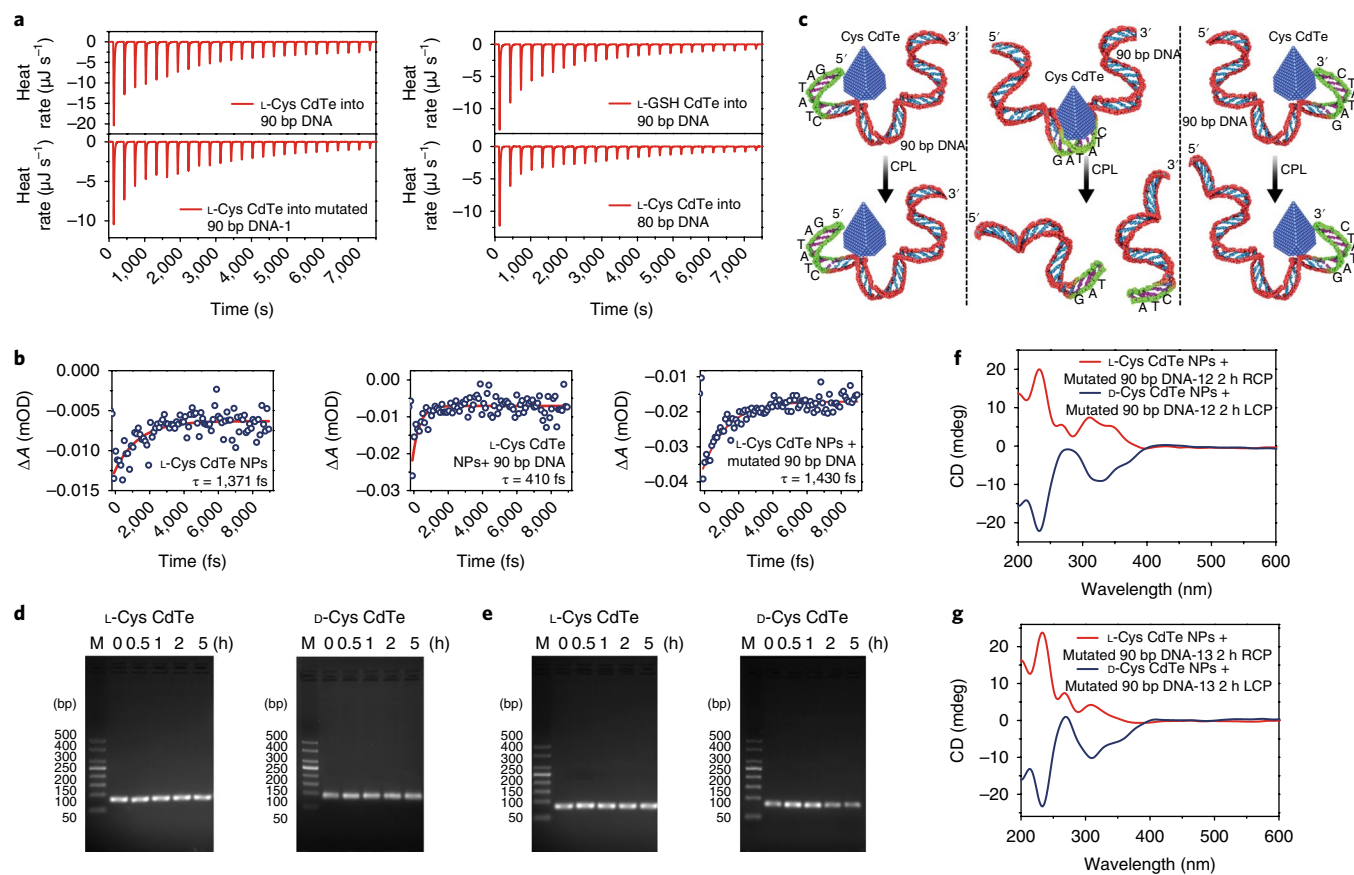
Fig. 4 | Specific binding and conformational change between target DNA and chiral nanoparticles. a, ITC data for 90 bp DNA and L-Cys CdTe nanoparticles, mutated 90 bp DNA-1 and L-Cys CdTe nanoparticles, 90 bp DNA and L-GSH CdTe nanoparticles, and 80 bp DNA and L-Cys CdTe nanoparticles. **b**, Transient absorption spectra of L-Cys CdTe nanoparticles, L-Cys CdTe nanoparticles with 90 bp DNA and L-Cys CdTe nanoparticles with mutated 90 bp DNA-1. Blue dots indicate the differential absorbance of samples and the red line is the fitting curve. **c**, Schematic diagram of the conformational change in 90 bp DNA interacting with Cys-modified CdTe. The recognition sequence was located at the 5' or 3' end of the DNA, respectively. **d,e**, Electrophoresis images of Cys CdTe nanoparticles illuminated with mutated 90 bp DNA-12 (recognition sequence at 5' end) (**d**) and mutated 90 bp DNA-13 (recognition sequence at 3' end) (**e**). **f,g**, CD spectra of L-Cys CdTe and D-Cys CdTe nanoparticles mixed with mutated 90 bp DNA-12 (**f**) and mutated 90 bp DNA-13 (**g**) then illuminated under 405 nm RCP/LCP for 2 h. All experiments were performed in triplicate.

was located in the middle of the DNA (Fig. 3c), confirming that the mutated 90 bp DNA was not cut under these conditions. The ITC data show that the binding constant is rather weak between the mutated 90 bp DNA and the L- or D-Cys CdTe: $(2.64 \pm 0.39) \times 10^3\,M^{-1}$ or $(2.53 \pm 0.45) \times 10^3\,M^{-1}$, respectively, for mutated 90 bp DNA-12, and $(2.13 \pm 0.28) \times 10^3\,M^{-1}$ or $(2.53 \pm 0.34) \times 10^3\,M^{-1}$, respectively, for mutated 90 bp DNA-13 (Supplementary Figs. 92 and 93). A positive control was included, in which all the non-specific sequences in the 90 bp DNA fragment were altered, but the GAT′ATC in the middle was retained. The results showed that the DNA (with binding constants of $(1.25 \pm 0.39) \times 10^5\,M^{-1}$ or $(1.24 \pm 0.43) \times 10^5\,M^{-1}$ for L- and D-Cys nanoparticles) was gradually cleaved, indicating that the recognition sequence GAT′ATC in the middle of the 90 bp DNA exerts a conformational variation during DNA scission (Supplementary Figs. 94–97). With respect to the experimental evidence of a tetrahedral shape (Fig. 2b), several previous works have provided evidence that small nanoparticles with zinc-blende structure have a truncated tetrahedral shape, and the edges and apices have greatly preferred binding constants with specific sequences of DNA[27,42–44]. This finding further indicates the significance of the flexibility of the alternating A and T bases in the recognition sequence.

Mechanism of DNA cleavage. It has recently been reported that reactive oxygen species (ROS) are critical for both selective oxidation

and DNA lesions, and may therefore play major roles in our catalytic system[45,46]. Therefore, we used a 2′,7′-dichlorodihydrofluorescein (DCFH) probe to monitor ROS production by the DNA-combined chiral nanoparticles during irradiation (Fig. 5a and Supplementary Fig. 98)[47]. Simultaneously with DNA cleavage and nanorod formation, the ROS content in the 90 bp DNA solution increased in response to light over time. However, when the mutated 90 bp DNA was combined with the chiral nanoparticles, there was no ROS response to CPL exposure for 5 h (Supplementary Fig. 99). The same negative results were obtained with the 80 bp DNA and the GSH-modified nanoparticles (Supplementary Figs. 100 and 101). To exclude the possible effects of the DNA, a control experiment using the 90 bp DNA and a ROS inhibitor (NaN$_3$) was performed, and no changes in the ROS levels or DNA cleavage were observed (Fig. 5c and Supplementary Fig. 102). Therefore, ROS are crucial for DNA cleavage in our system. It is known that DNA sequences are connected by a phosphodiester bond between bases[48]. As shown in Fig. 5d, the selective DNA cleavage in our experiment indicates that the phosphodiester bond between bases T and A is broken through photoinduced ROS oxidation. To identify the kinds of ROS that cause the final DNA cleavage, assays of the main ROS species were performed. Figure 5a,b and Supplementary Figs. 103 and 104 present the data for singlet oxygen, superoxide and hydroxyl radical production when the chiral nanoparticles are combined with 90 bp
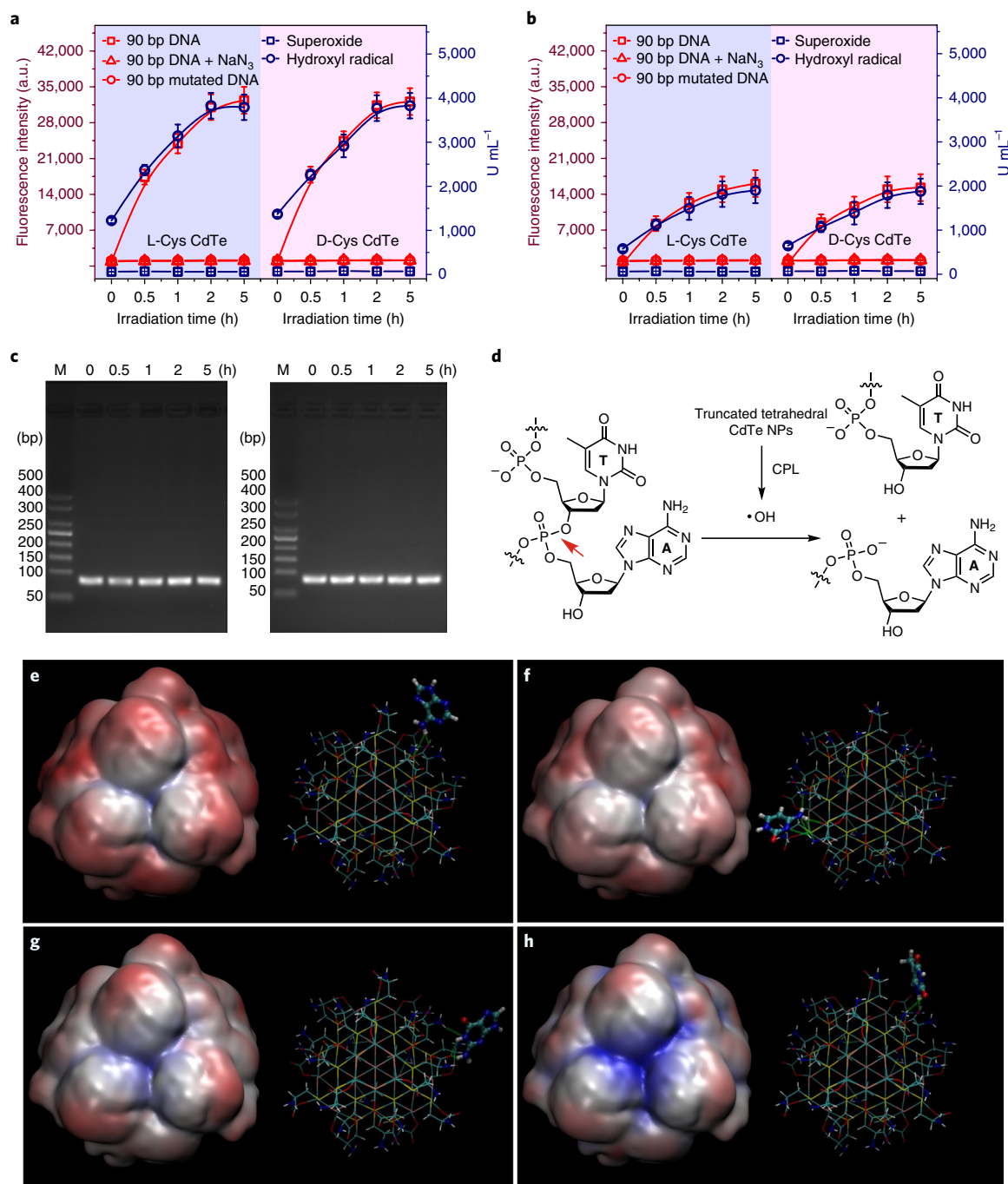
Fig. 5 | Mechanism of DNA cleavage. a, ROS-induced DNA cleavage. Statistical chart of ROS production and hydroxyl radical and superoxide production in L-Cys CdTe nanoparticles under RCP and D-Cys CdTe nanoparticles under LCP. **b**, L-Cys CdTe nanoparticles under LCP and D-Cys CdTe nanoparticles under RCP illuminated with 90 bp DNA, mutated 90 bp DNA and 90 bp DNA with ROS inhibitor (NaN$_3$) for 0–5 h. **c**, Electrophoresis images of L-Cys CdTe nanoparticles (left) and D-Cys CdTe nanoparticles (right) illuminated with 90 bp DNA with ROS inhibitor under 405 nm RCP/LCP for 5 h. Experiments were performed in triplicate. **d**, DNA shearing model of Cys CdTe nanoparticles, where the red arrow indicates the cleaved bond. **e–h**, Free energy landscapes (left) and most probable DNA base adsorbed on the model nanoparticle (right). Most negative free energy values are shown as red regions, and most positive values are shown as blue regions. Helmholtz free energy of adsorption for the most stable base–nanoparticle complex, and corresponding probability of this lowest-lying structure: adenine ($\Delta_{ads}A = -54.2$ kJ mol^{-1}, $P = 0.51$) (**e**); cytosine ($\Delta_{ads}A = -54.9$ kJ mol^{-1}, $P = 0.996$) (**f**); guanine ($\Delta_{ads}A = -52.8$ kJ mol^{-1}, $P = 0.77$) (**g**); thymine ($\Delta_{ads}A = -52.0$ kJ mol^{-1}, $P = 0.70$) (**h**). Error bars in **a** and **b** are mean ± s.d. ($n = 3$ independent samples).

DNA. Significantly, only the hydroxyl radical content in both the D-Cys- and L-Cys-modified nanoparticle mixtures increased under LCP and RCP illumination. The chiral CdTe nanoparticles displayed specific nuclease-mimetic activity under the corresponding CPL. To determine the differences in the reaction rate when the same

enantiomer was exposed to different polarized light scattering, the ROS levels produced by D-Cys or L-Cys nanoparticles under RCP or LCP activation were monitored (Fig. 5b). ROS production by the chiral nanoparticles was clearly affected by the different polarization directions with the same exposure time (Supplementary
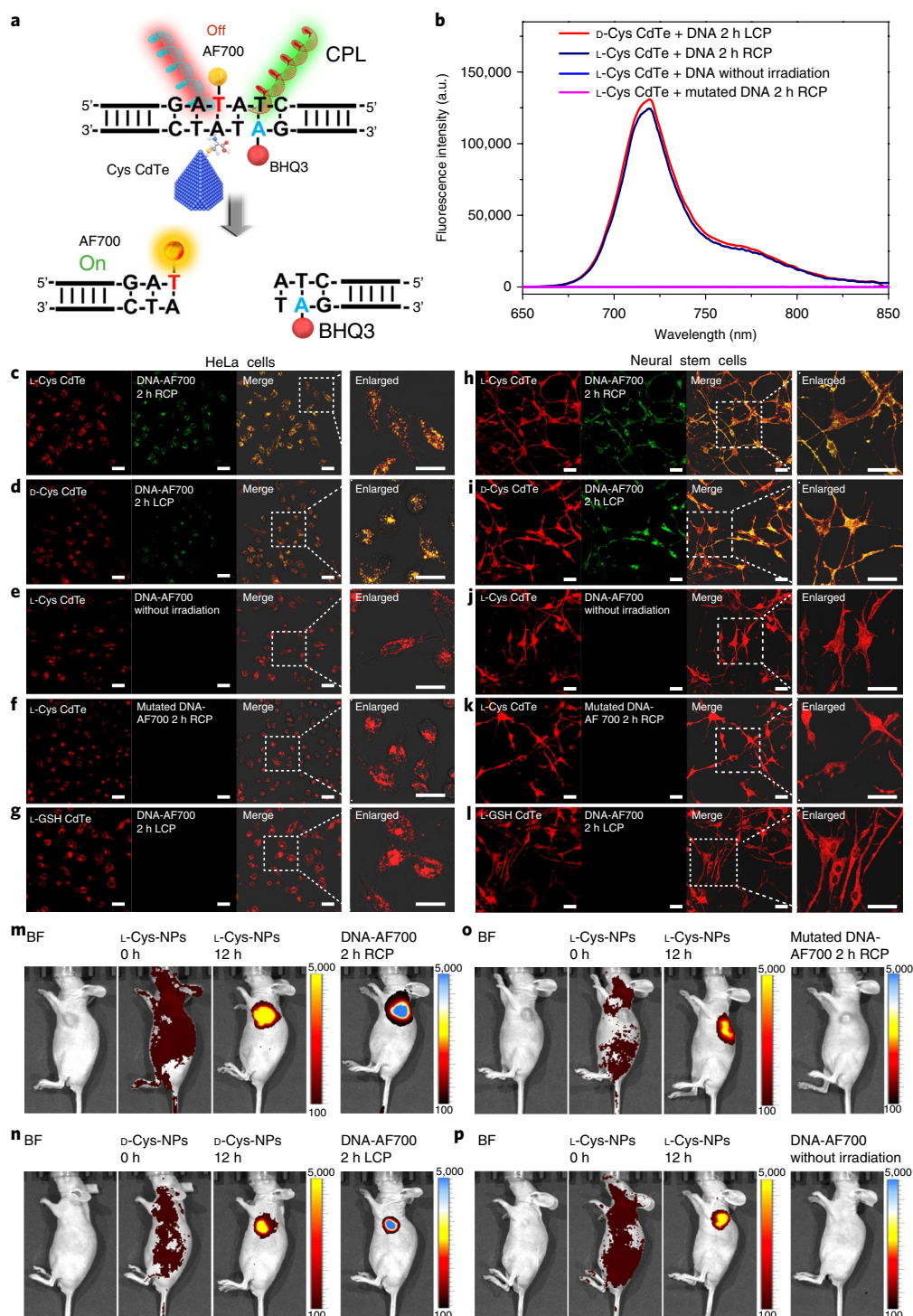
Fig. 6 | Photoinduced DNA cleavage in living cells and in vivo. a, Model of intracellular molecular beacon-tagged DNA shearing by Cys CdTe nanoparticles. **b**, Fluorescence of AF700-labelled 90 bp DNA after illumination with ʟ-Cys CdTe and ᴅ-Cys CdTe. **c,h**, Confocal images of ʟ-Cys CdTe nanoparticles incubated with HeLa cells (**c**) and neural stem cells (**h**) for 5 h (cells were transfected with AF700-labelled 90 bp DNA) and then irradiated with RCP for 2 h. **d,i**, Confocal images of ᴅ-Cys CdTe nanoparticles incubated with HeLa cells (**d**) and neural stem cells (**i**) for 5 h (cells were transfected with AF700-labelled 90 bp DNA) and then irradiated with LCP for 2 h. **e,j**, Confocal images of ʟ-Cys CdTe nanoparticles incubated with HeLa cells (**e**) and neural stem cells (**j**) for 5 h (cells were transfected with AF700-labelled mutated 90 bp DNA-1) without irradiation. **f,k**, Confocal images of ʟ-Cys CdTe nanoparticles incubated with HeLa cells (**f**) and neural stem cells (**k**) for 5 h (cells were transfected with AF700-labelled mutated 90 bp DNA-1) and then irradiated with RCP for 2 h. **g,l**, Confocal images of ʟ-GSH CdTe nanoparticles incubated withHeLa cells (**g**) and neural stem cells (**l**) for 5 h (cells were transfected with AF700-labelled 90 bp DNA) and then irradiated with LCP for 2 h. Scale bars, 20 µm. **m,n**, In vivo imaging of nude mice after ʟ-Cys CdTe nanoparticles (**m**) and ᴅ-Cys CdTe nanoparticles (**n**) injection for 0–12 h (the mice were transfected with AF700-labelled 90 bp DNA before injection) and irradiated under RCP or LCP for 2 h. **o**, In vivo imaging of nude mice after ʟ-Cys CdTe nanoparticles injection for 0–12 h (mice were transfected with AF700-labelled mutated 90 bp DNA-1 before injection) and irradiated under RCP for 2 h. **p**, In vivo imaging of nude mice after ʟ-Cys CdTe nanoparticles injection for 0–12 h (mice were transfected with AF700-labelled 90 bp DNA before injection) without irradiation. All experiments were performed in triplicate.

Figs. 105–107). Therefore, we compared the cleavage rates of the chiral nanoparticles under different CPL. Consistent with the ROS yield, the electrophoresis results showed that the L-Cys nanoparticles had a higher cleavage rate under RCP than under LCP, and the D-Cys nanoparticle rates were opposite (Supplementary Figs. 108–117). This difference can be attributed to the differential absorption efficiency of the chiral nanoparticles under CPL[49]. Four lambda DNA sequences were performed to confirm the specific cutting of Cys-modified CdTe (Supplementary Fig. 118 and Supplementary Tables 5–8). The experiments showed that the chiral semiconductor nanoparticle could be applied to the DNA selective scission in fragment length, site, and sequence specific through the chiral ligand of Cys recognition. It was also revealed that the nanoparticles, as electron donors, induced ROS generation, while the DNA was the receptor, leading to phosphodiester bond cleavage.

DNA selective cleavage simulation. We devised a modelling strategy by using quantum chemically calculated interaction energies within a standard statistical mechanics framework (Supplementary Figs. 119–137). The free energy landscapes provide direct evidence for the preferential adsorption of A and T on the same groove along the edge, closer to the middle of the nearest face of the tetrahedral nanoparticle than to the nearest corner, while C and G were found preferably in different hot spots, both closer to the nearest corner than to the middle of the nearest face. Thus, the GAT'ATC sequence contains a central segment of four consecutive bases that have a large affinity for the same groove along the edge of the nanoparticle, while the two termini of this sequence are expected to be found closer to the corners at both ends of the nanoparticle edge (Fig. 5e–h and Supplementary Figs. 138 and 139). The results indicate that the Cys-modified CdTe nanoparticles could specifically target the recognition sequence of GAT'ATC within the DNA helix.

The cleavage process was theoretically investigated with density functional theory (DFT) calculations (Supplementary Figs. 140–143). The results definitively show that the DNA could be efficiently cleaved after complementary attachment to the Cys-modified CdTe.

Photoinduced DNA cleavage in living cells and in vivo. To explore the endonuclease activity in a complex physiological environment, we utilized this photoactivated DNA cutting system in living cells and in vivo. The 90 bp DNA fragment was labelled with a molecular beacon (fluorescent dye Alexa Fluor 700 (AF700) and a quencher [BHQ3]) at the recognition site to visualize the whole cleavage process with fluorescent signals (Fig. 6a)[50]. When polyethylene glycol (PEG)-coated chiral CdTe nanoparticles (emission at 620 nm) were used, cell viability was over 90% after incubation for 24 h (Supplementary Fig. 144). Following exposure to CPL for 2 h, the cutting system produced an intense fluorescent signal at 720 nm, indicating the successful cleavage of the DNA in vitro (Fig. 6b). However, the mutated DNA sequence produced no fluorescent signal under the same conditions (Supplementary Fig. 145). Human cervical cancer cells (HeLa, ATCC CCL-2) and rat fetal neural stem cells (stem cells (neural), Gibco N7744100) were transfected with the labelled 90 bp DNA and then incubated with the PEG-coated chiral CdTe for 5 h, respectively (Supplementary Fig. 146). Intracellular fluorescence was tracked with confocal microscopy after CPL exposure for 2 h. As the incubation time increased, the intensity of the AF700 fluorescence from the specific cleavage fragments under CPL irradiation increased markedly, and co-localized with the corresponding nanoparticles (Fig. 6c,d,h,i). Notably, no AF700 fluorescence was recorded after any incubation period without irradiation (Fig. 6e,j). Consistent with the in vitro results, cells containing the mutated 90 bp DNA or with the molecular beacon tagged at a non-cleavage site or with GSH CdTe displayed almost no signal in the AF700 channel (720 nm) (Fig. 6f,g,k,l and Supplementary Figs. 147 and 148). These results demonstrate that

the recovered fluorescence originated from specific DNA scission in living cells by the chiral nanoparticles. In addition, we examined the chiral nanoparticles with bio-TEM after the photoinduced reaction. Interestingly, the nanoparticles combined with the 90 bp DNA in living cells were transformed into nanorods, whereas the nanoparticles remained unchanged when the cells contained the mutated 90 bp DNA sequence (Supplementary Figs. 149–154). To further confirm the feasibility of the photoactivated DNA cleavage system in vivo, HeLa tumour-bearing nude mice were prepared and transfected with the 90 bp DNA molecular beacon. The mice were then intravenously injected with the chiral nanoparticles. Nanoparticle fluorescence was recorded in the in vivo imaging system, and showed that the nanoparticles had accumulated at the tumour site 12 h after injection (Supplementary Fig. 155). To directly assess the effects of DNA cleavage on the tumour, the mice were exposed to 660 nm CPL for 2 h. Fluorescence at 720 nm was observed as an intensive signal at the tumour site, indicating that the DNA in the tumour was effectively cut by both the D-Cys- and L-Cys-modified nanoparticles (Fig. 6m,n). No signal was observed in the mutated DNA group or without irradiation, which strongly demonstrates that the fluorescence was induced by photoinduced DNA cleavage (Fig. 6o,p and Supplementary Fig. 156). The experimental data confirm that the developed photoactive chiral nanoparticles can be successfully applied in living cells and in vivo as biomimetic endonucleases to cut DNA with the presented fragment length, site and specificity.

Conclusion

We have developed a novel biomimetic sequence-specific DNAzyme reaction with Cys-modified nanoparticles under CPL. The findings show that DNA over 90 bp can be specifically and efficiently cleaved between bases T and A at the recognition site GAT'ATC, while the nanoparticles are transformed into Te-rich nanorods, with a distinct change in CD signal. Significantly, this work shows that the photoinduced DNA cutting platform performs well in vivo, with high efficiency and biocompatibility. Our findings provide new insights into the interactions between biomolecules and chiral nanomaterials, which will undoubtedly open up new applications for abiotic materials as novel tools in gene analysis, manipulation and life science.

Methods

Synthesis of D- or L-Cys stabilized CdTe nanoparticles. Briefly, the precursor solution was prepared by the reaction of 0.05 g of Al_2Te_3 with 4 ml of 0.5 M H_2SO_4 (strictly protected under a N_2 atmosphere). The precursor gas (H_2Te) generated was then passed through 0.985 g of $Cd(ClO_4)_2 \cdot 6H_2O$ in 125 ml of water containing 3 ml of 1 M D- or L-Cys/GSH as the stabilizing agent. The optimized pH of 12 was adjusted with a 1 M solution of NaOH under a nitrogen-saturated atmosphere. The reaction mixture was then refluxed at 110 °C in an oil bath under N_2 gas for 8 h. The flow rate of the N_2 gas was accurately maintained at 100 ml min⁻¹ during the entire synthesis process. The chiral CdTe nanoparticles obtained were purified by centrifugation with 2-propanol and resuspended in phosphate-buffered saline (PBS; 0.01 M, pH 7.4) for further use.

DNA cleavage by chiral Cys stabilized CdTe nanoparticles. DNAs were suspended in deionized water to a final concentration of 100 μM. DNA (50 μl of 1 μM) was mixed with 50 μl of 50 μM newly synthesized chiral nanoparticles in PBS solution. The mixture was then illuminated with CPL for different times in a quartz cuvette with an optical path length of 1 cm. A 405 nm laser was used as the light source, and the laser emission was transformed to CPL by directing it through a linear polarizer and a quarter-wave plate with a ±45° transmission angle.

Agarose gel electrophoresis. Agarose gel electrophoresis was performed as follows. After the DNA samples were illuminated with the chiral nanoparticles, they were separated by ultrafiltration centrifugation (3 kDa MWCO Millipore) in PBS. The purified DNA samples (10 μl) in PBS were then mixed with 2 μl of loading buffer and separated on 1.7% (for 1,839 bp DNA) or 3% (for 90 bp DNA) agarose gel in 0.5× TBE buffer containing ethidium bromide. Electrophoresis was performed at 100 V for 50 min. Electrophoretic images were captured with a Bio-Rad GelDoc XR System with Imaging Lab software.

Photoactivated DNA cleavage system in vivo. All animal procedures were performed according to institutional ethical guidelines and were approved by the Committee on Animal Welfare of Jiangnan University. The HeLa-tumour-bearing mice were randomly divided into different groups (five mice per group), and then intravenously injected with AF700-labelled 90 bp DNA or AF700-labelled mutated 90 bp DNA with the transfection reagent Invivofectamine 3.0 Reagent (Thermo Fisher Scientific). Briefly, 100 μl of 5 mM DNA in PBS was gently mixed with 100 μl of transfection reagent. The mixture was diluted sixfold and 200 μl was injected into each mouse at the tumour site. PEG-coated chiral nanoparticles (100 nM) were intravenously injected into the mice and the fluorescence was recorded at different time points with the 620 nm channel of an IVIS Spectrum In Vivo Imaging System (PerkinElmer). At 12 h after injection, the nanoparticles had accumulated at the tumour site. A 660 nm laser was used as the light source, and the laser emission was transformed to CPL by directing it through a linear polarizer and a quarter-wave plate with a ±45° transmission angle. The mice were then irradiated under RCP or LCP for 2 h, and fluorescence was recorded at 720 nm.

Reporting summary. Further information on experimental design is available in the Nature Research Reporting Summary linked to this article.

Data availability. The data supporting the findings of this study are available within the paper and its Supplementary Information and are available from the corresponding author upon reasonable request.

References

1. Jones, M. R., Seeman, N. C. & Mirkin, C. A. Nanomaterials. Programmable materials and the nature of the DNA bond. *Science* **347**, 1260901 (2015).
2. Yang, M. et al. Self-assembly of nanoparticles into biomimetic capsid-like nanoshells. *Nat. Chem.* **9**, 287–294 (2017).
3. Mao, L. B. et al. Synthetic nacre by predesigned matrix-directed mineralization. *Science* **354**, 107–110 (2016).
4. Pelaz, B. et al. The state of nanoparticle-based nanoscience and biotechnology: progress, promises, and challenges. *ACS Nano* **6**, 8468–8483 (2012).
5. Fan, K. et al. Magnetoferritin nanoparticles for targeting and visualizing tumour tissues. *Nat. Nanotech.* **7**, 459–464 (2012).
6. Wang, X. Y., Hu, Y. H. & Wei, H. Nanozymes in bionanotechnology: from sensing to therapeutics and beyond. *Inorg. Chem. Front.* **3**, 41–60 (2016).
7. Aiba, Y., Sumaoka, J. & Komiyama, M. Artificial DNA cutters for DNA manipulation and genome engineering. *Chem. Soc. Rev.* **40**, 5657–5668 (2011).
8. Xiao, X. J., Wu, T. B., Gu, F. D. & Zhao, M. P. Generation of artificial sequence-specific nucleases via a preassembled inert-template. *Chem. Sci.* **7**, 2051–2057 (2016).
9. Liu, B., Sun, Z., Huang, P. J. & Liu, J. Hydrogen peroxide displacing DNA from nanoceria: mechanism and detection of glucose in serum. *J. Am. Chem. Soc.* **137**, 1290–1295 (2015).
10. Liu, Y. et al. Biomimetic enzyme nanocomplexes and their use as antidotes and preventive measures for alcohol intoxication. *Nat. Nanotech.* **8**, 187–192 (2013).
11. Tonga, G. Y. et al. Supramolecular regulation of bioorthogonal catalysis in cells using nanoparticle-embedded transition metal catalysts. *Nat. Chem.* **7**, 597–603 (2015).
12. Rouge, J. L. et al. Ribozyme–spherical nucleic acids. *J. Am. Chem. Soc.* **137**, 10528–10531 (2015).
13. Sun, H. J. et al. Deciphering a nanocarbon-based artificial peroxidase: chemical identification of the catalytically active and substrate-binding sites on graphene quantum dots. *Angew. Chem. Int. Ed.* **54**, 7176–7180 (2015).
14. Huang, Y. et al. Self-assembly of multi-nanozymes to mimic an intracellular antioxidant defense system. *Angew. Chem. Int. Ed.* **55**, 6646–6650 (2016).
15. Zetsche, B. et al. Cpf1 is a single RNA-guided endonuclease of a Class 2 CRISPR-Cas system. *Cell* **163**, 759–771 (2015).
16. Loenen, W. A., Dryden, D. T., Raleigh, E. A., Wilson, G. G. & Murray, N. E. Highlights of the DNA cutters: a short history of the restriction enzymes. *Nucleic Acids Res.* **42**, 3–19 (2014).
17. Xu, Z., Zan, H., Pone, E. J., Mai, T. & Casali, P. Immunoglobulin class-switch DNA recombination: induction, targeting and beyond. *Nat. Rev. Immunol.* **12**, 517–531 (2012).
18. Cong, L. et al. Multiplex genome engineering using CRISPR/Cas systems. *Science* **339**, 819–823 (2013).
19. Roberts, R. J., Vincze, T., Posfai, J. & Macelis, D. REBASE—a database for DNA restriction and modification: enzymes, genes and genomes. *Nucleic Acids Res.* **43**, D298–D299 (2014).
20. Kameshima, W. et al. Conjugation of peptide nucleic acid with a pyrrole/ imidazole polyamide to specifically recognize and cleave DNA. *Angew. Chem. Int. Ed.* **52**, 13681–13684 (2013).
21. Wang, X., Sun, G., Li, N. & Chen, P. Quantum dots derived from two-dimensional materials and their applications for catalysis and energy. *Chem. Soc. Rev.* **45**, 2239–2262 (2016).
22. Bhatia, D. et al. Quantum dot-loaded monofunctionalized DNA icosahedra for single-particle tracking of endocytic pathways. *Nat. Nanotech.* **11**, 1112–1119 (2016).
23. Zrazhevskiy, P. & Gao, X. Quantum dot imaging platform for single-cell molecular profiling. *Nat. Commun.* **4**, 1619 (2013).
24. Yan, W. et al. Self-assembly of chiral nanoparticle pyramids with strong *R/S* optical activity. *J. Am. Chem. Soc.* **134**, 15114–15121 (2012).
25. Wang, Y., Fedin, I., Zhang, H. & Talapin, D. V. Direct optical lithography of functional inorganic nanomaterials. *Science* **357**, 385–388 (2017).
26. Li, S. et al. Dual-mode ultrasensitive quantification of microRNA in living cells by chiroplasmonic nanopyramids self-assembled from gold and upconversion nanoparticles. *J. Am. Chem. Soc.* **138**, 306–312 (2016).
27. Yeom, J. et al. Chiral templating of self-assembling nanostructures by circularly polarized light. *Nat. Mater.* **14**, 66–72 (2014).
28. Zhao, X. et al. Gold–quantum dot core–satellite assemblies for lighting up microRNA in vitro and in vivo. *Small* **12**, 4662–4668 (2016).
29. Li, X. B. et al. Self-assembled framework enhances electronic communication of ultrasmall-sized nanoparticles for exceptional solar hydrogen evolution. *J. Am. Chem. Soc.* **139**, 4789–4796 (2017).
30. Feng, W. et al. Assembly of mesoscale helices with near-unity enantiomeric excess and light–matter interactions for chiral semiconductors. *Sci. Adv.* **3**, e1601159 (2017).
31. Hendry, E. et al. Ultrasensitive detection and characterization of biomolecules using superchiral fields. *Nat. Nanotech.* **5**, 783–787 (2010).
32. Kotov, N. A. Inorganic nanoparticles as protein mimics. *Science* **330**, 188–189 (2010).
33. Ma, W. et al. Chiral inorganic nanostructures. *Chem. Rev.* **117**, 8041–8093 (2017).
34. Zhou, Y. L., Yang, M., Sun, K., Tang, Z. Y. & Kotov, N. A. Similar topological origin of chiral centers in organic and nanoscale inorganic structures: effect of stabilizer chirality on optical isomerism and growth of CdTe nanocrystals. *J. Am. Chem. Soc.* **132**, 6006–6013 (2010).
35. Boersma, A. J. et al. Catalytic enantioselective syn hydration of enones in water using a DNA-based catalyst. *Nat. Chem.* **2**, 991–995 (2010).
36. Mukhina, M. V. et al. Intrinsic chirality of CdSe/ZnS quantum dots and quantum rods. *Nano Lett.* **15**, 2844–2851 (2015).
37. Gao, F. L. et al. A singlet oxygen generating agent by chirality-dependent plasmonic shell–satellite nanoassembly. *Adv. Mater.* **29**, 1606864 (2017).
38. Lesnyak, V., Gaponik, N. & Eychmuller, A. Colloidal semiconductor nanocrystals: the aqueous approach. *Chem. Soc. Rev.* **42**, 2905–2929 (2013).
39. Burns, J. R., Seifert, A., Fertig, N. & Howorka, S. A biomimetic DNA-based channel for the ligand-controlled transport of charged molecular cargo across a biological membrane. *Nat. Nanotech.* **11**, 152–156 (2016).
40. Kim, Y., Geiger, J. H., Hahn, S. & Sigler, P. B. Crystal structure of a yeast TBP/TATA-box complex. *Nature* **365**, 512–520 (1993).
41. Yan, Z. & Wang, J. SPA-LN: a scoring function of ligand–nucleic acid interactions via optimizing both specificity and affinity. *Nucleic Acids Res.* **45**, e110 (2017).
42. Tang, Z. Y., Zhang, Z. L., Wang, Y., Glotzer, S. C. & Kotov, N. A. Self-assembly of CdTe nanocrystals into free-floating sheets. *Science* **314**, 274–278 (2006).
43. Boles, M. A. & Talapin, D. V. Self-assembly of tetrahedral CdSe nanocrystals: effective 'patchiness' via anisotropic steric interaction. *J. Am. Chem. Soc.* **136**, 5868–5871 (2014).
44. Yang, Y. A., Wu, H. M., Williams, K. R. & Cao, Y. C. Synthesis of CdSe and CdTe nanocrystals without precursor injection. *Angew. Chem. Int. Ed.* **44**, 6712–6715 (2005).
45. Chen, Y. Z. et al. Singlet oxygen-engaged selective photo-oxidation over Pt nanocrystals/porphyrinic MOF: the roles of photothermal effect and Pt electronic state. *J. Am. Chem. Soc.* **139**, 2035–2044 (2017).
46. Li, H. et al. New reaction pathway induced by plasmon for selective benzyl alcohol oxidation on BiOCl possessing oxygen vacancies. *J. Am. Chem. Soc.* **139**, 3513–3521 (2017).
47. Xue, T. et al. Integration of molecular and enzymatic catalysts on graphene for biomimetic generation of antithrombotic species. *Nat. Commun.* **5**, 3200 (2014).
48. Chandrasekar, J. & Silverman, S. K. Catalytic DNA with phosphatase activity. *Proc. Natl Acad. Sci. USA* **110**, 5315–5320 (2013).
49. Sun, M. et al. Intracellular localization of nanoparticle dimers by chirality reversal. *Nat. Commun.* **8**, 1847 (2017).
50. Zheng, J. et al. Rationally designed molecular beacons for bioanalytical and biomedical applications. *Chem. Soc. Rev.* **44**, 3036 (2015).

Author contributions

H.K., N.A.K. and C.X. conceived the project and designed the experiments. M.S. was responsible for DNA cutting and spectroscopic measurements. L.X. and A.Q. carried out cell and ITC experiments. T.H. and A.Q. were responsible for chiral CdTe nanoparticles synthesis and DNA electrophoresis. W.M. and C.H. carried out synchrotron small-angle X-ray scattering, X-ray photoelectron spectroscopy and transient absorption spectrum experiments. F.M.C and A.F.M. developed the models for free energy calculation. P.Z. and X.W. developed the DFT model. H.K. and M.S. carried out the studies in vivo. H.K. conceptualized the work. C.X. supervised the study and N.A.K. provided advice regarding the idea. H.K. and C.X. analysed the results and wrote the manuscript. H.K., C.X. and N.A.K. discussed the results and commented on the manuscript.

Competing interests

The authors declare no competing interests.

Additional information

Supplementary information is available for this paper at https://doi.org/10.1038/s41557-018-0083-y.

Reprints and permissions information is available at www.nature.com/reprints.

Correspondence and requests for materials should be addressed to H.K.

Publisher's note: Springer Nature remains neutral with regard to jurisdictional claims in published maps and institutional affiliations.

nature research

Corresponding author(s): Hua Kuang

Reporting Summary

Nature Research wishes to improve the reproducibility of the work that we publish. This form provides structure for consistency and transparency in reporting. For further information on Nature Research policies, see Authors & Referees and the Editorial Policy Checklist.

Statistical parameters

When statistical analyses are reported, confirm that the following items are present in the relevant location (e.g. figure legend, table legend, main text, or Methods section).

n/a	Confirmed	
☐	☒	The exact sample size (*n*) for each experimental group/condition, given as a discrete number and unit of measurement
☐	☒	An indication of whether measurements were taken from distinct samples or whether the same sample was measured repeatedly
☐	☒	The statistical test(s) used AND whether they are one- or two-sided *Only common tests should be described solely by name; describe more complex techniques in the Methods section.*
☐	☒	A description of all covariates tested
☐	☒	A description of any assumptions or corrections, such as tests of normality and adjustment for multiple comparisons
☒	☐	A full description of the statistics including central tendency (e.g. means) or other basic estimates (e.g. regression coefficient) AND variation (e.g. standard deviation) or associated estimates of uncertainty (e.g. confidence intervals)
☒	☐	For null hypothesis testing, the test statistic (e.g. *F*, *t*, *r*) with confidence intervals, effect sizes, degrees of freedom and *P* value noted *Give P values as exact values whenever suitable.*
☒	☐	For Bayesian analysis, information on the choice of priors and Markov chain Monte Carlo settings
☒	☐	For hierarchical and complex designs, identification of the appropriate level for tests and full reporting of outcomes
☒	☐	Estimates of effect sizes (e.g. Cohen's *d*, Pearson's *r*), indicating how they were calculated
☐	☒	Clearly defined error bars *State explicitly what error bars represent (e.g. SD, SE, CI)*

Our web collection on statistics for biologists may be useful.

Software and code

Policy information about availability of computer code

Data collection	Gatan Microscopy Suite Software, Lieca LAS AF Lite, Living Image, Imaging Lab, ITC run, Chirascan
Data analysis	OriginPro 8.5, NanoAnalyze(TA), Microsoft excel

For manuscripts utilizing custom algorithms or software that are central to the research but not yet described in published literature, software must be made available to editors/reviewers upon request. We strongly encourage code deposition in a community repository (e.g. GitHub). See the Nature Research guidelines for submitting code & software for further information.

Data

Policy information about availability of data

All manuscripts must include a data availability statement. This statement should provide the following information, where applicable:

- Accession codes, unique identifiers, or web links for publicly available datasets
- A list of figures that have associated raw data
- A description of any restrictions on data availability

The data supporting the findings of this study are available within the paper and its Supplementary Information files and are available from the corresponding author upon reasonable request.

Field-specific reporting

Please select the best fit for your research. If you are not sure, read the appropriate sections before making your selection.

☒ Life sciences ☐ Behavioural & social sciences

For a reference copy of the document with all sections, see nature.com/authors/policies/ReportingSummary-flat.pdf

Life sciences

Study design

All studies must disclose on these points even when the disclosure is negative.

Sample size	All the experiments were performed in three replicated or more. Sample sizes for experiments were estimated based on previous experience with a similar setup that showed significance. For cell experiments, we used 3 independent cell cultures and approx. 5000000 cells were collected for each sample. Statistics were derived when at least 3 independent samples were analyzed. Experiments involving mice were performed three times with 5 animals being analysed in each experiment.
Data exclusions	No data was excluded from the analyses.
Replication	The experimental findings can be reliably reproduced. All experiments in this study were replicated at least three times.
Randomization	The mice applied in this experiment were randomly selecting and divided into different groups, each group contain five mice.
Blinding	The investigators were blinded to group allocation during data collection and/or analysis. All samples were analyzed using the reported approach without prior knowledge of their levels.

Materials & experimental systems

Policy information about availability of materials

n/a	Involved in the study
☒	☐ Unique materials
☒	☐ Antibodies
☐	☒ Eukaryotic cell lines
☐	☒ Research animals
☒	☐ Human research participants

Unique materials

Obtaining unique materials	No unique materials were used in these experiments.

Antibodies

Antibodies used	No antibodies were used in these experiments.
Validation	No antibodies were used in these experiments.

Eukaryotic cell lines

Policy information about cell lines

Cell line source(s)	HeLa cell line in this experiment was obtained from Shanghai Institutes for Biological Sciences, Shanghai, China. Neural stem cell line were purchased from Thermo Fisher Scientific, Shanghai, China.
Authentication	No cell lines authentication was performed.
Mycoplasma contamination	No testing for mycoplasma contamination was performed.
Commonly misidentified lines (See ICLAC register)	No commonly misidentified cell lines were used.

Research animals

Animals/animal-derived materials	All animal studies were performed according to institutional ethical guidelines and were approved by the Committee on Animal Welfare of Jiangnan University.Female nude mice (5 weeks old, weight 16.3± 2.1 g) were obtained from Qinglong Mountain Animal Technology(Nanjing, China). Before the experiment, the mice were raised for 3 days at 28℃ with feed and water under aseptic conditions. Then, the mice were randomly divided into groups for further experiment.

Human research participants

Population characteristics	No human research participants in these experiments.

Method-specific reporting

n/a	Involved in the study
☒	☐ ChIP-seq
☒	☐ Flow cytometry
☒	☐ Magnetic resonance imaging

ChIP-seq

Data deposition

☐ Confirm that both raw and final processed data have been deposited in a public database such as GEO.

☐ Confirm that you have deposited or provided access to graph files (e.g. BED files) for the called peaks.

Data access links *May remain private before publication.*	No ChIP-seq were used in this experiment.
Files in database submission	No ChIP-seq were used in this experiment.
Genome browser session (e.g. UCSC)	No ChIP-seq were used in this experiment.

Methodology

Replicates	No ChIP-seq were used in this experiment.
Sequencing depth	No ChIP-seq were used in this experiment.
Antibodies	No ChIP-seq were used in this experiment.
Peak calling parameters	No ChIP-seq were used in this experiment.
Data quality	No ChIP-seq were used in this experiment.
Software	No ChIP-seq were used in this experiment.

Flow Cytometry

Plots

Confirm that:

☐ The axis labels state the marker and fluorochrome used (e.g. CD4-FITC).

☐ The axis scales are clearly visible. Include numbers along axes only for bottom left plot of group (a 'group' is an analysis of identical markers).

☐ All plots are contour plots with outliers or pseudocolor plots.

☐ A numerical value for number of cells or percentage (with statistics) is provided.

Methodology

Sample preparation	No Flow Cytometry were used in this experiment.
Instrument	No Flow Cytometry were used in this experiment.

Software	No Flow Cytometry were used in this experiment.
Cell population abundance	No Flow Cytometry were used in this experiment.
Gating strategy	No Flow Cytometry were used in this experiment.

☐ Tick this box to confirm that a figure exemplifying the gating strategy is provided in the Supplementary Information.

Magnetic resonance imaging

Experimental design

Design type	No Magnetic resonance imaging were used in this experiment.
Design specifications	No Magnetic resonance imaging were used in this experiment.
Behavioral performance measures	No Magnetic resonance imaging were used in this experiment.

Acquisition

Imaging type(s)	No Magnetic resonance imaging were used in this experiment.
Field strength	No Magnetic resonance imaging were used in this experiment.
Sequence & imaging parameters	No Magnetic resonance imaging were used in this experiment.
Area of acquisition	No Magnetic resonance imaging were used in this experiment.

Diffusion MRI ☐ Used ☐ Not used

Preprocessing

Preprocessing software	No Magnetic resonance imaging were used in this experiment.
Normalization	No Magnetic resonance imaging were used in this experiment.
Normalization template	No Magnetic resonance imaging were used in this experiment.
Noise and artifact removal	No Magnetic resonance imaging were used in this experiment.
Volume censoring	No Magnetic resonance imaging were used in this experiment.

Statistical modeling & inference

Model type and settings	No Magnetic resonance imaging were used in this experiment.
Effect(s) tested	No Magnetic resonance imaging were used in this experiment.

Specify type of analysis: ☐ Whole brain ☐ ROI-based ☐ Both

Statistic type for inference (See Eklund et al. 2016)	No Magnetic resonance imaging were used in this experiment.
Correction	No Magnetic resonance imaging were used in this experiment.

Models & analysis

n/a	Involved in the study
☐	☐ Functional and/or effective connectivity
☐	☐ Graph analysis
☐	☐ Multivariate modeling or predictive analysis

Functional and/or effective connectivity	No Magnetic resonance imaging were used in this experiment.
Graph analysis	No Magnetic resonance imaging were used in this experiment.
Multivariate modeling and predictive analysis	No Magnetic resonance imaging were used in this experiment.

Behavioural & social sciences

Study design

All studies must disclose on these points even when the disclosure is negative.

Study description	No Behavioural & social sciences were studied in this experiment.
Research sample	No Behavioural & social sciences were studied in this experiment.
Sampling strategy	No Behavioural & social sciences were studied in this experiment.
Data collection	No Behavioural & social sciences were studied in this experiment.
Timing	No Behavioural & social sciences were studied in this experiment.
Data exclusions	No Behavioural & social sciences were studied in this experiment.
Non-participation	No Behavioural & social sciences were studied in this experiment.
Randomization	No Behavioural & social sciences were studied in this experiment.